

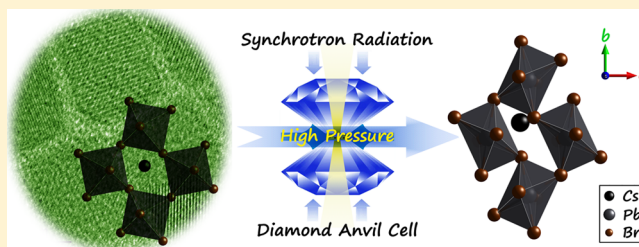
# Pressure Effects on Structure and Optical Properties in Cesium Lead Bromide Perovskite Nanocrystals

Guanjun Xiao,<sup>b</sup> Ye Cao, Guangyu Qi, Lingrui Wang, Chuang Liu, Zhiwei Ma, Xinyi Yang, Yongming Sui, Weitao Zheng, and Bo Zou<sup>\*b</sup>

State Key Laboratory of Superhard Materials, College of Materials Science and Engineering, Jilin University, Changchun 130012, People's Republic of China

## S Supporting Information

**ABSTRACT:** Metal halide perovskites (MHPs) are gaining increasing interest because of their extraordinary performance in optoelectronic devices and solar cells. However, developing an effective strategy for achieving the band-gap engineering of MHPs that will satisfy the practical applications remains a great challenge. In this study, high pressure is introduced to tailor the optical and structural properties of MHP-based cesium lead bromide nanocrystals (CsPbBr<sub>3</sub> NCs), which exhibit excellent thermodynamic stability. Both the pressure-dependent steady-state photoluminescence and absorption spectra experience a stark discontinuity at ~1.2 GPa, where an isostructural phase transformation regarding the *Pbnm* space group occurs. The physical origin points to the repulsive force impact due to the overlap between the valence electron charge clouds of neighboring layers. Simultaneous band-gap narrowing and carrier-lifetime prolongation of CsPbBr<sub>3</sub> trihalide perovskite NCs were also achieved as expected, which facilitates the broader solar spectrum absorption for photovoltaic applications. Note that the values of the phase change interval and band-gap red-shift of CsPbBr<sub>3</sub> nanowires are between those for CsPbBr<sub>3</sub> nanocubes and the corresponding bulk counterparts, which results from the unique geometrical morphology effect. First-principles calculations unravel that the band-gap engineering is governed by orbital interactions within the inorganic Pb–Br frame through structural modification. Changes of band structures are attributed to the synergistic effect of pressure-induced modulations of the Br–Pb bond length and Pb–Br–Pb bond angle for the PbBr<sub>6</sub> octahedral framework. Furthermore, the significant distortion of the lead–bromide octahedron to accommodate the Jahn–Teller effect at much higher pressure would eventually lead to a direct to indirect band-gap electronic transition. This study enables high pressure as a robust tool to control the structure and band gap of CsPbBr<sub>3</sub> NCs, thus providing insight into the microscopic physiochemical mechanism of these compressed MHP nanosystems.



## INTRODUCTION

Metal halide perovskites (MHPs) have attracted considerable attention for their applications in solar cells with high power conversion efficiency.<sup>1</sup> The intriguing optical properties and the prospect for low-cost device fabrication promote the rapid development of MHPs. In particular, the recent success of organometallic halide perovskites in photovoltaic devices has triggered research activities on inorganic halide perovskite nanocrystals (NCs) due to their good stability, ultrahigh photoluminescence (PL) quantum yield, and composition-dependent luminescence with a wide color gamut.<sup>2–4</sup> The cesium lead bromide (CsPbBr<sub>3</sub>) perovskites deliver outstanding optoelectronic properties and are significantly more stable than organic–inorganic hybrid perovskite compounds. Restricting the physical dimensions of the CsPbBr<sub>3</sub> perovskite crystallites to a nanometer region would further unlock spatial confinement effects. This change allows large spectral tunability, thus facilitating the band-gap optimization for the devices.<sup>5–10</sup>

Pressure, as a unique thermodynamic variable, provides a powerful means to study the structural and electronic behaviors of MHP materials. The loading of pressure by a diamond anvil

cell (DAC) can lead to a close packing and reduce the interatomic distances, which would profoundly modify electronic orbitals and bonding patterns.<sup>11–14</sup> In recent years, high-pressure studies on MHP materials have set off a new wave of upsurge.<sup>15–19</sup> Significant progress in the pressure response of methylammonium/formamidinium-based lead halide perovskites has recently been made by several independent groups.<sup>20,21</sup> However, most high-pressure objects were confined to the organometallic halide perovskites, whose instability and sensitivity to oxygen/water largely limit actual photovoltaic applications.<sup>22–28</sup>

In this regard, we devoted efforts to imposing pressure on an all-inorganic halide perovskite nanosystem, CsPbBr<sub>3</sub> NCs, which exhibit a relatively good thermodynamic stability. The pressure-driven structure and optical properties of this material were characterized by the combination of *in situ* time-resolved carrier dynamics, angle dispersive synchrotron X-ray diffraction, and optical spectroscopy measurements. All of the high-

Received: May 22, 2017

Published: July 6, 2017

pressure experimental results indicated that CsPbBr<sub>3</sub> NCs experienced an isostructural phase transformation regarding the *P6mm* space group at approximately 1.2 GPa. The physical origin was dictated by the repulsive force impact, owing to the overlap between valence electron charge clouds of neighboring layers. Time-resolved PL decay indicates a significant prolongation of carrier lifetime under high pressure. We further investigated the geometrical morphology effects on the values of phase change interval and band-gap red-shift under high pressure among CsPbBr<sub>3</sub> nanocubes, nanowires, and the corresponding bulk counterparts. Theoretical computations predicted that orbital interactions associated with the variations of Br–Pb bond lengths and the shrinkage of Pb–Br–Pb bond angles within the lead–bromide octahedral motif were simultaneously responsible for the pressure-induced structural modulation and band-gap shift. Upon further compression, the original structure theoretically showed the tendency to adopt an indirect band-gap configuration, owing to the great distortion of PbBr<sub>6</sub> octahedra resulting from the Jahn–Teller effect at much higher pressure. Our findings represented the fundamental relationship between structural variations and optoelectronic properties of CsPbBr<sub>3</sub> NCs, thereby providing insight into the microscopic physiochemical mechanism of the MHP nanosystem at extremes.

## EXPERIMENTAL SECTION

**Synthesis and Characterization of CsPbBr<sub>3</sub> NCs.** The targeted CsPbBr<sub>3</sub> NCs were synthesized according to the modulated colloidal chemistry method.<sup>6</sup> In a typical synthesis, cesium carbonate (0.407 g, Cs<sub>2</sub>CO<sub>3</sub>, Sigma-Aldrich, 99.9%) and oleic acid (1.2 mL, OA, Sigma-Aldrich, 90%) together with octadecene (20 mL, ODE, Sigma-Aldrich, 90%) were loaded in a 50 mL three-neck flask. After drying for 1 h at 120 °C, the solvent was heated under N<sub>2</sub> to 150 °C until all CsCO<sub>3</sub> powders were dissolved, indicating the formation of a Cs-oleate complex. Then, Cs-oleate was cooled to 100 °C before injection. Subsequently, 5 mL of ODE, 0.069 g of PbBr<sub>2</sub> (Sigma-Aldrich, 98%), 0.5 mL of oleylamine (OLA, Sigma-Aldrich, 70%), and 0.5 mL of OA were loaded in a 50 mL three-neck flask. The mixture was heated to 120 °C with strong stirring and remained for 1 h under N<sub>2</sub>. After complete solubilization of PbBr<sub>2</sub>, the temperature was raised to 170 °C, and the Cs-oleate solution (0.5 mL) was quickly injected. About 20 s later, the reaction mixture was extracted and quenched by toluene. The resultant mixture was isolated using toluene and excess acetone by centrifuging for 5 min at 10 000 rpm. The resulting samples were characterized by transmission electron microscopy (TEM), high-resolution TEM, high-angle annular dark-field scanning transmission electron microscopy (HAADF-STEM) images, and elemental mapping performed on a JEM-2200FS with an emission gun operating at 200 kV.

**In Situ High-Pressure Optical Experiments.** All of the *in situ* high-pressure experiments shown in this study were carried out with a symmetric DAC apparatus. Ila-type ultralow fluorescence diamonds with a culet size of 300 μm were used. A T301 stainless steel gasket was preindented by the diamonds and was drilled to generate a 100-μm-diameter cavity for loading the samples. Typically, the prepared CsPbBr<sub>3</sub> NCs were enclosed in the gasket hole together with a ruby ball for determining the actual pressure through the standard ruby fluorescence technique.<sup>29</sup> Therein, silicon oil with a viscosity of 10 cSt was utilized as the pressure transmitting medium (PTM), which was purchased from Dow Corning Corporation (South Saginaw Road, Midland, MI, USA). The high-pressure evolution of steady-state PL spectra was collected utilizing a modified spectrophotometer (Ocean Optics, QE65000). A semiconductor laser with an excitation wavelength of 355 nm was employed for all fluorescence experiments. Note that all the parameters are fixed completely over each high-pressure PL experiment to avoid the effects of different excitation laser intensities and luminous fluxes on the resulting PL intensity of intrinsic

CsPbBr<sub>3</sub> NCs. The pressure-dependent PL decay curves were obtained with a high-resolution nitrogen and dye laser (Photon Technology International, Inc.) as the excitation source ( $\lambda_{\text{exc}} = 481$  nm, 800 ps pulse width, 10 Hz repetition rate). Meanwhile, the *in situ* high-pressure absorption spectra of CsPbBr<sub>3</sub> NCs were recorded with an optical fiber spectrometer (Ocean Optics, QE65000) using a deuterium-halogen light source. *In situ* high-pressure angle-dispersive X-ray diffraction (ADXRD) patterns were obtained with a wavelength of 0.6199 Å at beamline 15U1, Shanghai Synchrotron Radiation Facility (SSRF), China. A focused beam size of about 4 × 3.5 μm<sup>2</sup> was adopted for data collection. CeO<sub>2</sub> was used as a standard sample for the calibration of geometric parameters. The Bragg diffraction rings were collected using a Mar-165 CCD detector with an average acquisition time of 10 s for each pressure and then were integrated on the basis of the FIT2D program, yielding 1D intensity versus diffraction angle 2-theta patterns.<sup>30</sup> All the high-pressure experiments were conducted at room temperature.

**Computation.** First-principles density functional theory (DFT) computations were performed using the plane-wave pseudopotential technique with the generalized gradient approximation (GGA), as implemented in the Cambridge serial total energy package (CASTEP).<sup>31</sup> A plane-wave basis set with an energy cutoff of 290 eV was used, and the Brillouin zone sampling for geometry optimizations was performed using a 5 × 5 × 3 Monkhorst–Pack *k*-point mesh. The convergence thresholds were set at values of 5.0 e<sup>−6</sup> eV/atom for energy and 10<sup>−2</sup> eV Å<sup>−1</sup> for force. The partial density of states (DOSs) of isolated atoms were collected by adopting the identical pseudopotential of the GGA that is implemented in the Vienna *ab initio* simulation package (VASP).<sup>32</sup>

## RESULTS AND DISCUSSION

The morphology and structure of the synthesized CsPbBr<sub>3</sub> NCs were investigated using TEM and HRTEM characterizations. As shown in Figure 1a and b, the samples before

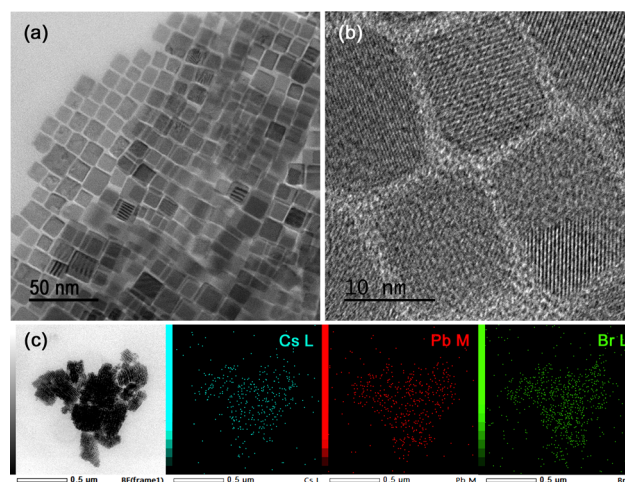


**Figure 1.** (a) TEM image and (b) high-resolution TEM image of CsPbBr<sub>3</sub> NCs before compression. (c) HAADF-STEM image and element mapping (Cs, Pb, and Br) of the as-prepared CsPbBr<sub>3</sub> NCs.

compression exhibit a nanocube morphology with good crystallinity. Elemental mapping indicates that the elements Cs, Pb, and Br are homogeneously distributed throughout the whole sample, which suggests high purity of the final products (Figure 1c). The corresponding size distribution of obtained CsPbBr<sub>3</sub> NCs with Gauss fitting is depicted in Figure S1. It shows that the CsPbBr<sub>3</sub> NCs have an average diameter of 11.7 nm, with a standard deviation of 1.9 nm. Then, the surface molecular decoration of synthesized CsPbBr<sub>3</sub> NCs was further

characterized. The OLA molecule,  $\text{CH}_3(\text{CH}_2)_7\text{CH}=\text{CH}(\text{CH}_2)_8\text{NH}_2$ , which has a buckled chain length of  $\sim 2.05$  nm (Scheme S1), often acts as a surfactant in NC synthesis as reported elsewhere. The Fourier transform infrared (FTIR) spectra of  $\text{CsPbBr}_3$  NCs were recorded with a PerkinElmer spectrometer (Spectrum One B). The FTIR spectra of  $\text{CsPbBr}_3$  NCs could be well assigned to the vibrational mode of the OLA molecule (Figure S2). In a word, the synthesized  $\text{CsPbBr}_3$  NCs are passivated by the organic ligand of OLA on the surface after the washing treatment. In addition, as one of the star materials utilized as promising optoelectronic materials for  $\text{CsPbBr}_3$  NCs, there is an urgent need to characterize the corresponding optical properties. Figure 2 depicts the PL spectrum of the as-

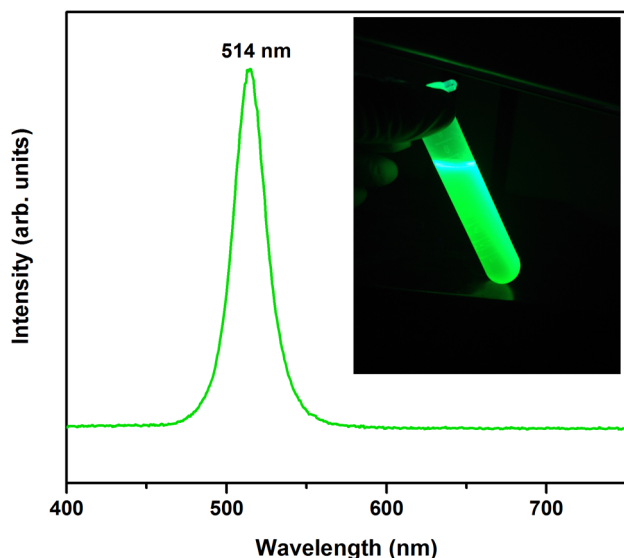


**Figure 2.** Ambient PL spectra of as-prepared  $\text{CsPbBr}_3$  NCs and the corresponding photograph of  $\text{CsPbBr}_3$  NCs under UV light.

prepared  $\text{CsPbBr}_3$  NCs and the optical photograph under UV light. It is found that the PL maximum is centered at  $\sim 514$  nm irradiated by a 355 nm laser under ambient conditions. The line-width of emission is as narrow as about 25 nm, which facilitates the high-resolution display technology. Under the irradiation of UV light, the  $\text{CsPbBr}_3$  NC colloid displays a bright green color.

Considering the outstanding optical properties of  $\text{CsPbBr}_3$  NCs, an *in situ* high-pressure PL measurement was performed. Selected steady-state PL spectra with increasing pressure and optical micrographs of the emission in the sample chamber are shown in Figure 3. The inset shows the schematic diagram of the symmetric DAC used in high-pressure experiments. Apparently, the PL peak displayed a red-shift in wavelength and gradually became broad with an increase in pressure. Additionally, the PL intensity decreased sharply upon compression to 1.21 GPa, after which the fluorescence was abruptly quenched, which may be governed by the structure-related change. Moreover, we plotted the PL intensity vs pressure and wavelength vs pressure of the synthesized  $\text{CsPbBr}_3$  NCs as shown in Figure S3 in the Supporting Information. It is found that the PL intensity of  $\text{CsPbBr}_3$  NCs decreased linearly with increasing pressure, whereas the PL location was linearly shifted to high wavelength under pressure. The optical photographs, with the assistance of a microscope, clearly reveal the darkening trend of the PL brightness in

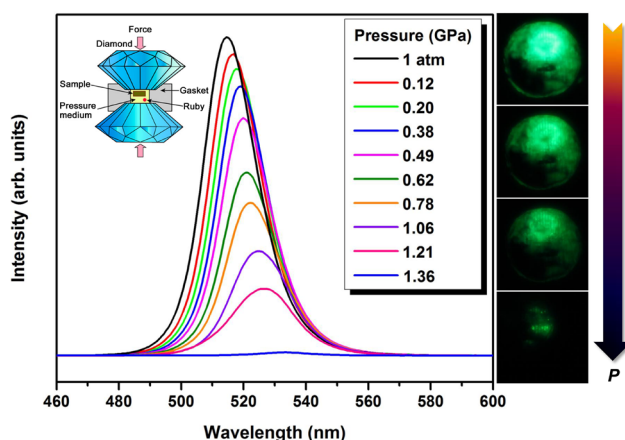


**Figure 3.** Pressure-dependent PL spectra of  $\text{CsPbBr}_3$  NCs. Inset shows the schematic diagram of a symmetric diamond anvil cell used in the high-pressure experiments. The right panel represents the microphotographs in the sample chamber at selected pressures of 1 atm and 0.49, 0.78, and 1.21 GPa irradiated by a 355 nm laser.

$\text{CsPbBr}_3$  NCs, accompanied by the color changes from bright green to dark green.

We further recorded the time-resolved PL decay dynamics of  $\text{CsPbBr}_3$  NCs to explore the exciton recombination rate at a laser of 481 nm under pressure. The schematic diagram of the lifetime measurement is shown in Figure S4. In principle, the observed lifetime profiles are the convolutional results of the real decay curves and the instrumental response function (IRF) to extract the time constant. The width of the IRF is generally determined to be less than 1 ns, thereby greatly facilitating the data fitting. As the external pressure approached about 1.03 GPa, the carrier lifetime fitted with an exponential formula underwent an obvious increase of  $\sim 19\%$  from 12.6 ns at ambience, implying a pressure-driven decrease in oscillator strength that agrees well with the changes of PL intensity (Figure 4a). Detailed lifetime data and the corresponding errors of  $\text{CsPbBr}_3$  nanocrystals under different pressure points are shown in Table S1. The prolonged lifetime of  $\text{CsPbBr}_3$  NCs is closely involved in surface-related trap states and is crucial to the long carrier diffusion length of these materials. This finding is highly beneficial to efficiently promote the photon-generated carrier charge separation in photovoltaic applications.<sup>33,34</sup> Typical time-resolved PL decay profiles at selected pressures are shown in Figure 4b. Due to the nearly quenched PL intensity at 1.28 GPa, the PL decay data of  $\text{CsPbBr}_3$  NCs were presented as discrete points so as not to reveal the lifetime profile by means of fitting. Upon decompression, the transient PL decay profile was recovered, indicating the reversibility of the phase transition.

The pressure-dependent absorption spectra of  $\text{CsPbBr}_3$  NCs measured in a DAC apparatus are collected in Figure S5. At ambient conditions, the sample exhibited an apparent absorbance at the band edge of 492 nm. Upon further compression, the absorption experienced a gradual red-shift below 1.19 GPa, followed by a stark blue jump until 2.25 GPa. The sudden change of the absorption spectra at 1.19 GPa was in accordance with the discontinuity in the PL spectra. The consistent variations of both the absorption and PL spectra should be correlated with the onset of phase transformation in  $\text{CsPbBr}_3$  NCs under high pressure. Upon the complete release of pressure, the absorption recovered to the initial position, suggesting the reversibility of the pressure-driven phase



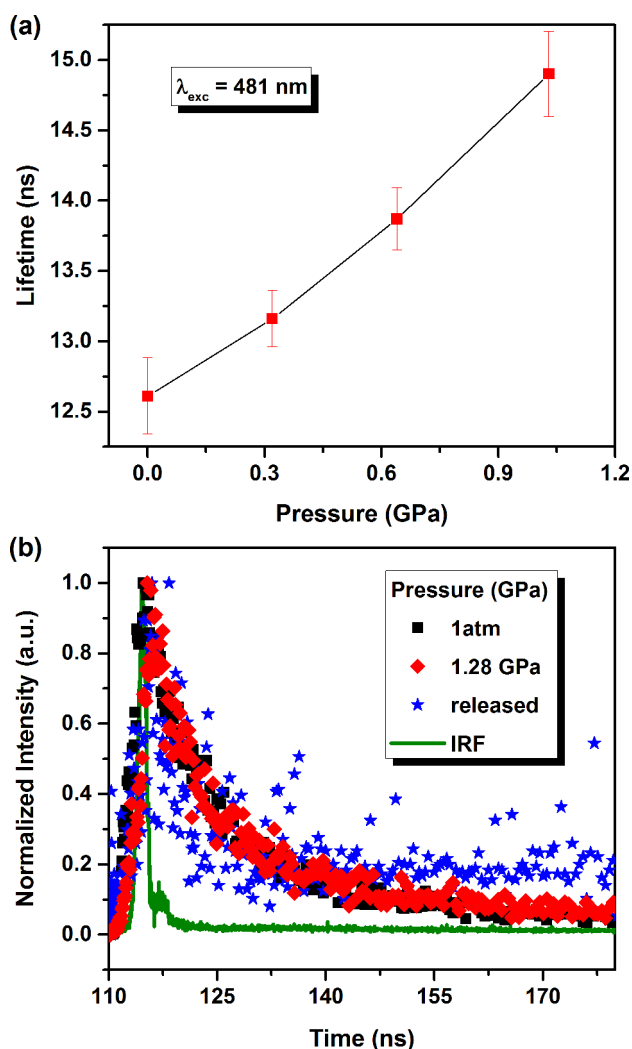


**Figure 4.** (a) Lifetime of CsPbBr<sub>3</sub> NCs as a function of pressure up to 1.03 GPa by using a high-resolution nitrogen and dye laser with an excitation wavelength of 481 nm. (b) Time-resolved PL decay profiles at selected pressures of 1 atm and 1.28 GPa and decompression, as well as the instrumental response function (IRF) curve.

transition. Detailed evolution of the band-gap energy for CsPbBr<sub>3</sub> NCs with increasing pressure is displayed in Figure 5. At relatively low pressure, the electronic band exhibited a linear narrowing by 0.11 eV from the initial 2.52 eV. With further compression, the rate of the photon energy presented a sharp increase between 1.19 and 1.45 GPa, where the pressure range of 0.26 GPa should be ascribed to the phase change interval. Thereafter, the band-gap energy underwent a successive increase up to 2.98 eV. Moreover, the band gaps at selected pressures are given through the extrapolation of the linear region to the energy axis intercept in terms of a Tauc plot (Figure S6).

Thus far, high-pressure modulation of the energy gap in CsPbBr<sub>3</sub> bulk materials has not yet been reported. We here obtained the pressure response of UV absorption and PL spectra in CsPbBr<sub>3</sub> bulk materials in order to make a comparison. As shown in Figures S7 and S8, the absorption spectrum of CsPbBr<sub>3</sub> bulk materials was initially red-shifted upon compression to 1.21 GPa. Thereafter, it exhibited a blue-shift to 2.03 GPa, at which a new phase peak appeared, denoted with an asterisk. The phase change interval of 0.82 GPa ranging

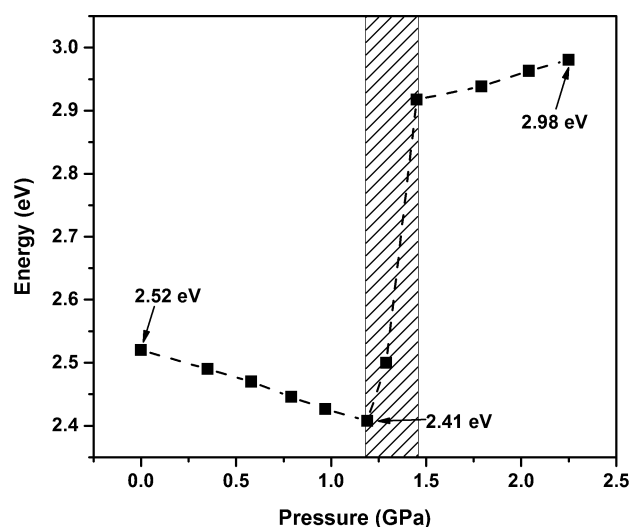


**Figure 5.** Shift of band-gap energy with increasing pressure. The shadow region indicates the phase transition interval.

from 1.21 to 2.03 GPa is significantly larger than that (0.26 GPa) of CsPbBr<sub>3</sub> NCs. On the contrary, the band-gap red-shift of 0.02 eV is far less than the corresponding CsPbBr<sub>3</sub> nanocubes (0.11 eV) presented in this study. The pressure-dependent PL spectra of CsPbBr<sub>3</sub> bulk materials underwent an initial red-shift and then a blue-shift until the PL intensity vanished with further compression. This trend in PL spectra is in accordance with the variations of absorption as a function of pressure. However, the blue-shift of the PL spectra in the present CsPbBr<sub>3</sub> nanocubes was not observed, which should be mainly attributed to the short phase change interval of CsPbBr<sub>3</sub> nanocubes with high surface energy.

Likewise, we further investigated the morphology effect of the compressed CsPbBr<sub>3</sub> NCs (nanocubes vs nanowires). In terms of the recent report by Yang et al.,<sup>8</sup> we successfully synthesized high-crystallinity CsPbBr<sub>3</sub> nanowires, as shown in Figure S9. The obtained CsPbBr<sub>3</sub> nanowires possess an average diameter of 12 nm, which is close to the dimension of the aforementioned CsPbBr<sub>3</sub> nanocubes. To make a comparison, we conducted the pressure-dependent UV absorption and PL spectra in the obtained CsPbBr<sub>3</sub> nanowires (Figures S10 and S11). It is found that the absorption and PL spectra underwent a similar trend with bulk materials as the pressure increased. The absorption spectrum of CsPbBr<sub>3</sub> nanowires was initially red-shifted upon compression to 1.22 GPa. Thereafter, a blue-shift occurred until 1.80 GPa, at which a new phase peak appeared, denoted with asterisk. The phase change interval of 0.58 GPa ranging from 1.22 to 1.80 GPa of CsPbBr<sub>3</sub> nanowires is larger than that (0.26 GPa) of CsPbBr<sub>3</sub> NCs, but smaller than that (0.82 GPa) of bulk materials, whereas the band-gap red-shift of 0.05 eV in CsPbBr<sub>3</sub> nanowires is less than the CsPbBr<sub>3</sub> nanocubes (0.11 eV), but greater than the corresponding bulk counterparts (0.02 eV). The pressure-dependent PL spectra of CsPbBr<sub>3</sub> nanowires experienced a similar change as compared with the CsPbBr<sub>3</sub> bulk materials under high pressure. Note that the values of the phase change interval and band-gap red-shift of CsPbBr<sub>3</sub> nanowires are between those for CsPbBr<sub>3</sub> nanocubes and the corresponding bulk counterparts, respectively. Obviously, the anisotropic wire-like morphology of CsPbBr<sub>3</sub> nanowires has a great impact on the pressure-induced variations. The unique geometrical shape of nanowires with anisotropic dimensions should be responsible for the

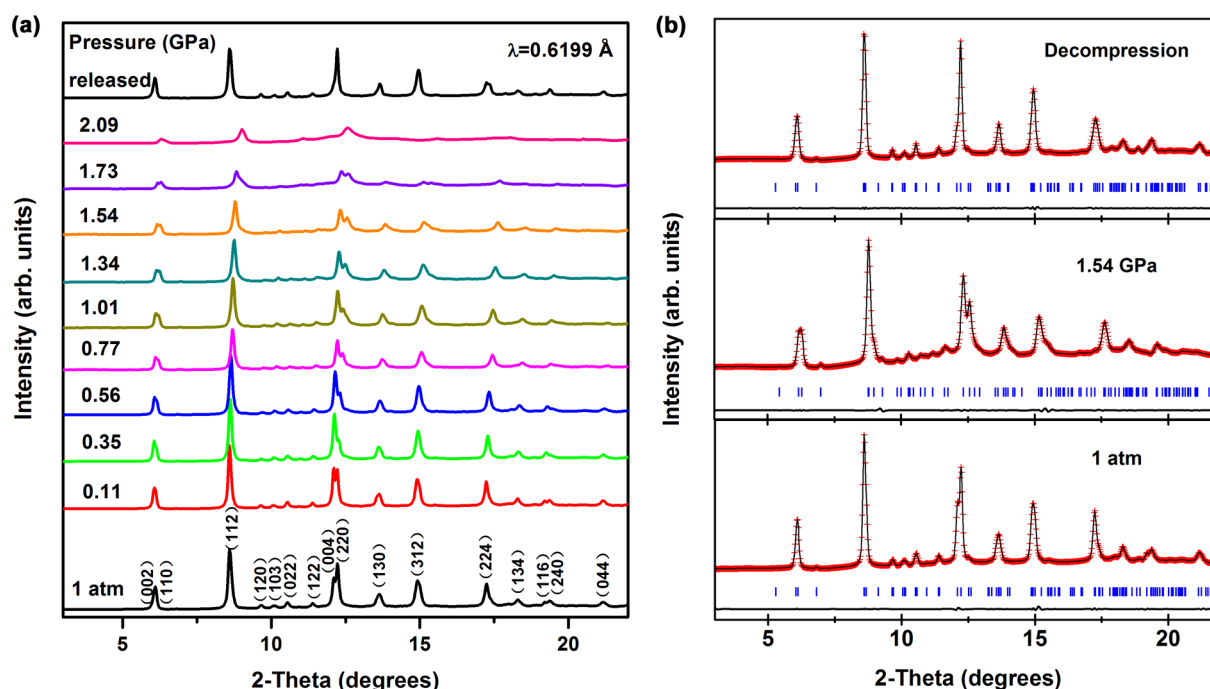


**Figure 6.** (a) Representative *in situ* ADXRD patterns of CsPbBr<sub>3</sub> NCs with the presence of silicon oil as PTM during the high-pressure experiments. (b) Refinements of the experimental (red fork), simulated (black profile), and difference (black line) ADXRD patterns at 1 atm and 1.54 GPa and quenched phase upon completely releasing the pressure to ambient conditions. Therein, blue vertical markers indicate the corresponding Bragg reflections.

phenomena, owing to the nanosized diameter and the length up to micrometers analogous to the bulk size.

As compared with the recent reports on pressure-induced fusion of CsPbBr<sub>3</sub> superlattices by Nagaoka et al.,<sup>19</sup> a completely distinct result was observed. Nagaoka et al. reported a blue-shift in PL wavelength with pressure in CsPbBr<sub>3</sub> superlattices, followed by a shift to longer wavelengths, whereas we observed an opposite trend with increasing pressure in our high-pressure experiments. The inflection point of the PL peak at 0.4 GPa, as described by Nagaoka et al., was attributed to the pure orthorhombic phase transition from the initial mixture including cubic and orthorhombic phases. Our initial structure was pure orthorhombic phase, which is recently corroborated by Brutchey et al. entitled “On the crystal structure of colloidal prepared CsPbBr<sub>3</sub> quantum dots”.<sup>35</sup> The work by Nagaoka et al. was mainly focused on the pressure-sintered, large, two-dimensional nanoplatelets from the initial CsPbBr<sub>3</sub> superlattices by *nonhydrostatic* pressure. Thus, the deviatoric stress effect resulting from the anisotropic pressure gradient should be considered. Therein, only pressure-dependent PL spectra were given without a deep understanding from the view of the atomic energy level. In this study, more comprehensive techniques, including *in situ* high-pressure-absorption, -PL, -lifetime, and -ADXRD measurements, were used to investigate the pressure-induced band gap and structure evolutions in the CsPbBr<sub>3</sub> nanocrystals. Therein, silicon oil, with a viscosity of 10 cSt, was utilized as the PTM to provide the perfect hydrostaticity.

In order to clarify the correlation between the optical properties and structure of CsPbBr<sub>3</sub> NCs in this study, *in situ* ADXRD experiments were carried out to provide more information about the crystal structure. Although the changes of PL and absorption spectra were obvious, the ADXRD patterns over pressures were hardly altered, except for a normal

shift to higher diffraction angles. When the pressure reached roughly 2.09 GPa, only a few broad diffraction peaks were detected, indicating that crystallinity is becoming worse and CsPbBr<sub>3</sub> NCs have the tendency to be amorphous at higher pressures. The overall observation of the ADXRD experiments indicated that CsPbBr<sub>3</sub> NCs displayed a regular reduction of the lattice parameters and did not experience a distinct structural variation during the whole compression up to 2.09 GPa. The refinements of the selected ADXRD patterns are depicted in Figure 6. It is observed that the refinement of the ADXRD pattern at 1.54 GPa matches the experimental data points very well ( $R_{wp} = 0.44\%$ ,  $R_p = 0.21\%$ ). This enables us to unambiguously determine the high-pressure phase to be orthorhombic with the *Pbnm* space group, possessing the same crystallographic system at 1 atm. Moreover, the corresponding lattice constants at 1.54 GPa are  $a = 7.96$  Å,  $b = 8.09$  Å, and  $c = 11.52$  Å. Note that the orthorhombic crystal structure could persist when the pressure was released to the ambient conditions.

To further analyze the structural evolution, the normalized lattice constants of CsPbBr<sub>3</sub> NCs as a function of pressure up to 2.25 GPa were elucidated (Figure S12). It was found that the pressure response of  $b$  and  $c$  axes for CsPbBr<sub>3</sub> NCs was similar, but the compressibility of the  $a$  axis was more sensitive to the pressure compared with the  $b$  and  $c$  axes. Meanwhile, the compressed rate happened to be a turning point for the  $b$  axis at above 1.34 GPa. Furthermore, the experimental pressure–volume ( $P$ – $V$ ) data (Figure 7) ranging from ambience to 2.25 GPa were fitted utilizing the following third-order Birch–Murnaghan equation of state:

$$P(V) = \frac{3B_0}{2} \left[ \left( \frac{V_0}{V} \right)^{7/3} - \left( \frac{V_0}{V} \right)^{5/3} \right] \left\{ 1 + \frac{3}{4} (B'_0 - 4) \left[ \left( \frac{V_0}{V} \right)^{2/3} - 1 \right] \right\}$$

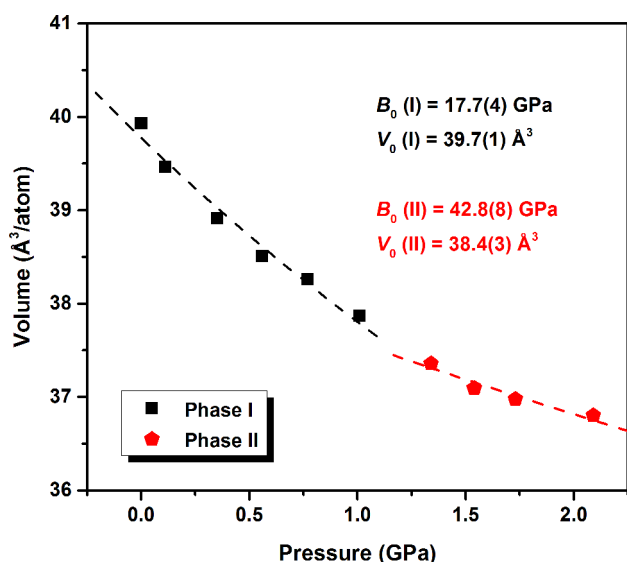


Figure 7. Pressure dependence of the unit cell volume of CsPbBr<sub>3</sub> NCs fitted by the third-order Birch–Murnaghan equation.

where  $V_0$  is the zero-pressure volume,  $B_0$  is the bulk modulus at ambient pressure, and  $B_0'$  is a parameter for the pressure derivative. No further discontinuities were apparent in the  $P$ – $V$  profile over the whole compression. Nevertheless, a significant change could be observed in compressibility between 1.0 and 1.3 GPa, which well agrees with the evolution of the absorption and PL spectra. Since the isostructural phase transitions are usually considered to originate from the electronic structural change in the matter, the as-prepared CsPbBr<sub>3</sub> NCs do undergo an isostructural phase transition.<sup>16,36</sup> The physical origin points to the repulsive force impact because of the overlap between the valence electron charge clouds of the neighboring layers.<sup>37</sup> With  $B_0'$  fixed at 4, the isothermal bulk modulus  $B_0$  for phase II of CsPbBr<sub>3</sub> NCs was estimated as 42.8(8) GPa, which is much larger than that of phase I (17.7(4) GPa). This finding indicates the highly difficult compressibility toward phase II. Moreover, the morphology and crystallinity of CsPbBr<sub>3</sub> NCs did not exhibit a distinct change before and after compressions, which could be readily deduced from the TEM and high-resolution TEM images, as shown in Figure S13.

First-principles calculations on CsPbBr<sub>3</sub> were employed to assess the response of the electronic structure to the external pressure. Figure S16 depicts the simulated band-gap energy with the increase of pressure. The calculated results in band-gap

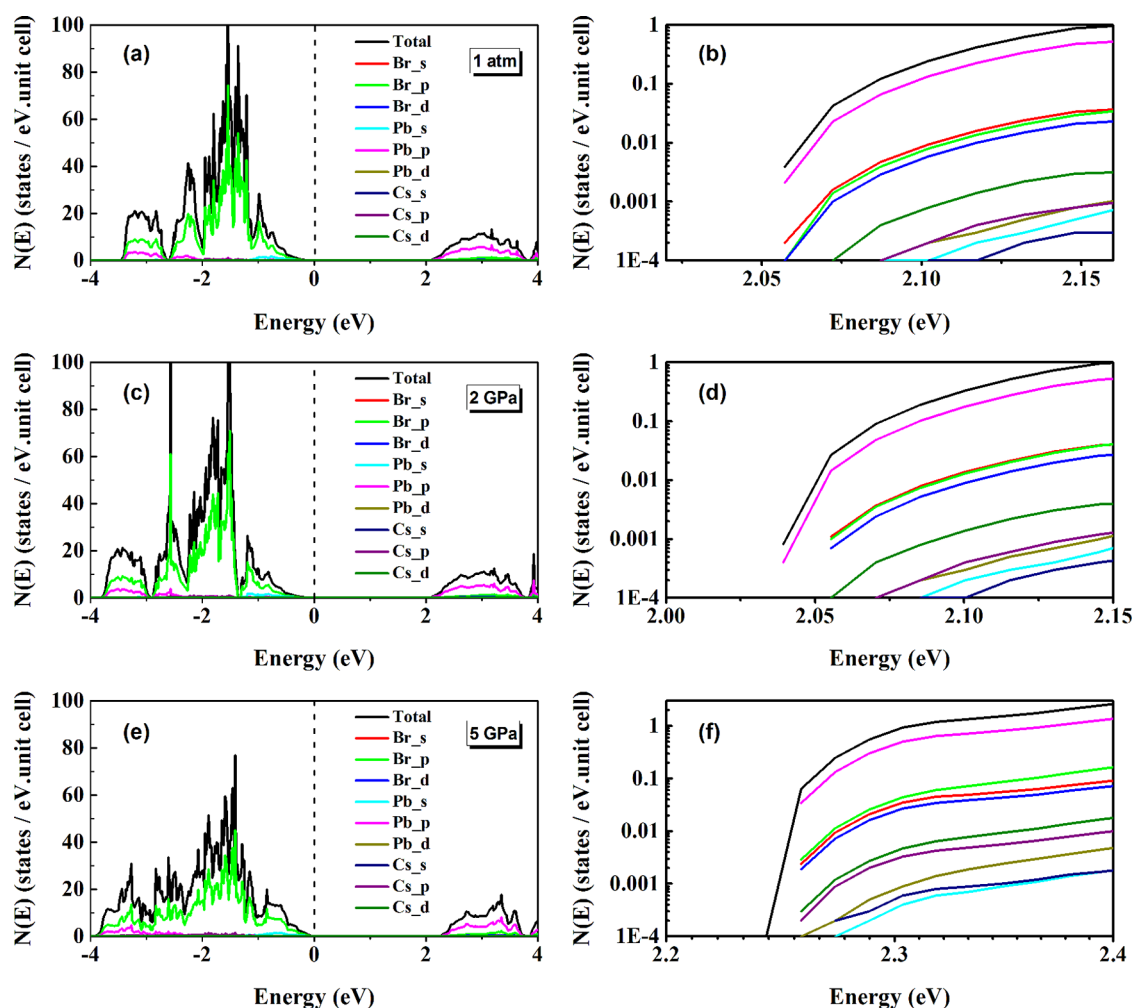
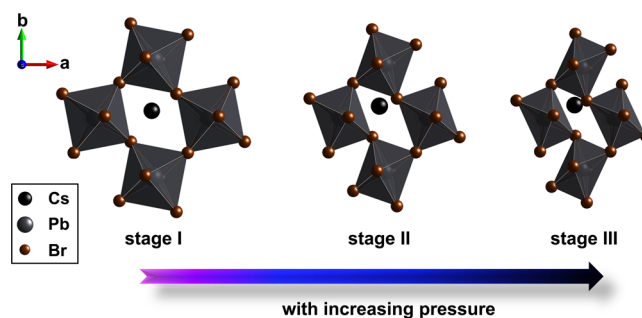


Figure 8. Total and partial density of states (DOSs) of isolated atoms for Cs, Pb, and Br atoms at 1 atm (a, b), 2 GPa (c, d), and 5 GPa (e, f). The transverse dashed line represents the Fermi level,  $E_F$ . Right panels of (b), (d), and (f) represent the corresponding enlarged views in the conduction band minimum region.

energy matched well with the experiments. Energies for both of them have the tendency to decrease in the low-pressure region, followed by the increase in the high-pressure range. Detailed theoretical energy band structures and density of states of CsPbBr<sub>3</sub> at selected pressures of 1 atm, 2 GPa, and 5 GPa are shown in Figure S17. The initial direct band-gap energy of 2.14 eV decreased to 2.04 eV as the pressure approached 2 GPa, after which the band-gap energy then exhibited an increase to 2.31 eV until 5 GPa. As the theoretical calculations were based on the corresponding bulk materials at 0 K under vacuum, different pressure points are normally observed between the experiments and computations (Figures S14 and S15). As is known, the band gap was exclusively distinguished by the separation of the conduction band minimum (CBM) and valence band maximum (VBM). The partial density of states, as shown in Figure 8, suggested that the CsPbBr<sub>3</sub> perovskites exhibited an inverted band structure, since the VBM was identified as the antibonding hybridization between the Pb 6s and Br 4p orbitals, whereas the CBM state was governed by the orbital interactions between Pb 6p and Br 4s orbitals in the [PbBr<sub>6</sub>]<sup>4-</sup> octahedral network. Note that the VBM state has almost a Br 4p character, owing to the higher energy level of the Br 4p orbital compared with that of the Pb 6s state. The CBM was almost totally contributed from the Pb 6p state, because the Pb 6p orbital possessed a much greater energy level than the Br 4s state. When pressure was applied to CsPbBr<sub>3</sub> perovskites, the CBM was mostly a nonbonding localized state of Pb 6p orbitals, which is less sensitive to external pressure stimulus. Therefore, the band-gap evolution of CsPbBr<sub>3</sub> perovskites was initially determined by the change of VBM when pressure is applied.<sup>38</sup> With the increase of pressure, the enhanced orbital coupling between the Pb 6s and Br 4p states pushed up the VBM due to its antibonding character, which explains the red-shift of the band gap with pressure. As the CsPbBr<sub>3</sub> trihalide perovskite was subjected to pressure beyond 2 GPa, the CBM happened to be dominated by the strong coupling of the Pb 6p and Br 4p orbitals. Accordingly, the blue jump can be interpreted from the significant shift to higher energy level of the CBM by the exertion of pressure, thereby leading to the widened band gap. When a much higher pressure of 7 GPa was applied, an electronic transition to indirect band gap was observed resulting from the VBM movement from the G point to the X point (Figure S18), which should be greatly correlated with the amorphous state of the CsPbBr<sub>3</sub> that appeared in the ADXRD patterns. Note that the indirect band-gap features of solar absorbers are known to be beneficial for low carrier recombination rates and thus long minority carrier diffusion lengths.<sup>39,40</sup> Although it was unable to determine the indirect band-gap nature from the present absorption spectrum at 7 GPa (Figure S19), our calculation indeed provided a possibility about the electronic structure evolution of CsPbBr<sub>3</sub> perovskites at considerably higher pressure.

For the inorganic trihalide perovskite of CsPbBr<sub>3</sub>, the divalent metal Pb cation is octahedrally coordinated by halide Br anions (Figure 9). There are three nonequivalent Pb–Br bonds and two nonequivalent Pb–Br–Pb angles within the PbBr<sub>6</sub> octahedral framework for the orthorhombic CsPbBr<sub>3</sub> crystal, as shown in Figure S20a. Before 2 GPa, all of the bond lengths and angles were shortened under high pressure, thereby resulting in a condensed lead–bromide octahedron (stage II in Figure 9). As a consequence, the optical properties are inevitably influenced by the redefinition of boundary conditions for the electronic wave functions owing to pressure-driven



**Figure 9.** Schematic illustrations with respect to polyhedral views of crystal structures of CsPbBr<sub>3</sub> perovskites under high pressure.

structure changes.<sup>41</sup> The reduction of bond lengths played a dominant role in the decrease of the band-gap energy. At above 2 GPa, the decreasing rate with pressure for all the Pb–Br bond lengths became slow, even presenting an apparent rising tendency for length 3 (Figure S20b). Meanwhile, an initial rise in the bond angle 2 was observed; then a decline in this angle occurred afterward. In stark contrast, the bond angle 1 throughout exhibited a significant drop, which contributed to the widened electronic band (Figure S20c). Upon further compression, the compound eventually evolved into an indirect band-gap structure as a result of the considerable distortion of the more compact octahedral skeleton to accommodate the Jahn–Teller effect (stage III in Figure 9). The results highly corroborate the strong relations between the band conformation and the crystal structure of CsPbBr<sub>3</sub> perovskites.

## CONCLUSIONS

The pressure-engineered structure and optical properties of CsPbBr<sub>3</sub> NCs were systematically investigated by means of a DAC apparatus. Combining the ADXRD patterns with *in situ* absorption, PL, and carrier lifetime against pressures, the CsPbBr<sub>3</sub> NCs indeed experienced an isostructural phase transition. Simultaneous band-gap narrowing and carrier-lifetime prolongation of CsPbBr<sub>3</sub> trihalide perovskites NCs were also achieved as expected. The unique geometrical morphology effect was responsible for the different values of phase change interval and band-gap red-shift among CsPbBr<sub>3</sub> nanocubes, nanowires, and the corresponding bulk counterparts. First-principles calculations demonstrated that the variations of band gaps were invoked for orbital interactions associated with the synergistic effects of the pressure-induced variations of Br–Pb bond length and Pb–Br–Pb bond angle within the PbBr<sub>6</sub> octahedral network. Furthermore, the significant deformation of the lead–bromide octahedron resulting from the Jahn–Teller effect at much higher pressure would ultimately give rise to a direct to indirect band-gap electronic transition. These findings provide insight into the microscopic physiochemical mechanism of these compressed MHP nanosystems, based on the tuning of structure and band gaps of CsPbBr<sub>3</sub> NCs under high pressure.

## ASSOCIATED CONTENT

### Supporting Information

The Supporting Information is available free of charge on the ACS Publications website at DOI: 10.1021/jacs.7b05260.

*In situ* high-pressure absorption spectra of CsPbBr<sub>3</sub> nanocubes, nanowires and the corresponding bulk counterpart, *in situ* high-pressure PL spectra of CsPbBr<sub>3</sub>



nanowires and the corresponding bulk counterpart, FTIR spectra, pressure-dependent lattice constants, TEM and high-resolution TEM images of CsPbBr<sub>3</sub> nanowires and CsPbBr<sub>3</sub> nanocubes after compression, simulated band structures with increasing pressure, bond lengths and angles within a lead–bromide octahedron as a function of pressure (PDF)

## AUTHOR INFORMATION

### Corresponding Author

\*zoubo@jlu.edu.cn

### ORCID

Guanjun Xiao: 0000-0002-7013-1378

Bo Zou: 0000-0002-3215-1255

### Notes

The authors declare no competing financial interest.

## ACKNOWLEDGMENTS

The authors gratefully acknowledge funding support from the National Natural Science Foundation of China (Nos. 21673100, 11404135, 11504126, and 91227202), Chang Jiang Scholars Program (No. T2016051), the China Postdoctoral Science Foundation (Nos. 2015T80295 and 2014M550171), Changbai Mountain Scholars Program (No. 2013007), and Jilin Provincial Science & Technology Development Program (No. 20150520087JH). The work concerning *in situ* ADXRD measurements was performed at beamline 15U1, Shanghai Synchrotron Radiation Facility (SSRF).

## DEDICATION

Dedicated to Prof. Guangtian Zou on the occasion of his 80th birthday.

## REFERENCES

- (1) Eperon, G. E.; Leijtens, T.; Bush, K. A.; Prasanna, R.; Green, T.; Wang, J. T.-W.; McMeekin, D. P.; Volonakis, G.; Milot, R. L.; May, R.; Palmstrom, A.; Slotcavage, D. J.; Belisle, R. A.; Patel, J. B.; Parrott, E. S.; Sutton, R. J.; Ma, W.; Moghadam, F.; Conings, B.; Babayigit, A.; Boyen, H.-G.; Bent, S.; Giustino, F.; Herz, L. M.; Johnston, M. B.; McGehee, M. D.; Snaith, H. J. *Science* **2016**, 354, 861.
- (2) Wang, Y.; Li, X.; Song, J.; Xiao, L.; Zeng, H.; Sun, H. *Adv. Mater.* **2015**, 27, 7101.
- (3) Song, J.; Li, J.; Li, X.; Xu, L.; Dong, Y.; Zeng, H. *Adv. Mater.* **2015**, 27, 7162.
- (4) Li, X.; Cao, F.; Yu, D.; Chen, J.; Sun, Z.; Shen, Y.; Zhu, Y.; Wang, L.; Wei, Y.; Wu, Y.; Zeng, H. *Small* **2017**, 13, 1603996.
- (5) Nedelcu, G.; Protesescu, L.; Yakunin, S.; Bodnarchuk, M. I.; Grotevent, M. J.; Kovalenko, M. V. *Nano Lett.* **2015**, 15, 5635.
- (6) Protesescu, L.; Yakunin, S.; Bodnarchuk, M. I.; Krieg, F.; Caputo, R.; Hendon, C. H.; Yang, R. X.; Walsh, A.; Kovalenko, M. V. *Nano Lett.* **2015**, 15, 3692.
- (7) Bekenstein, Y.; Koscher, B. A.; Eaton, S. W.; Yang, P.; Alivisatos, A. P. *J. Am. Chem. Soc.* **2015**, 137, 16008.
- (8) Zhang, D.; Eaton, S. W.; Yu, Y.; Dou, L.; Yang, P. *J. Am. Chem. Soc.* **2015**, 137, 9230.
- (9) Zhang, D.; Yang, Y.; Bekenstein, Y.; Yu, Y.; Gibson, N. A.; Wong, A. B.; Eaton, S. W.; Kornienko, N.; Kong, Q.; Lai, M.; Alivisatos, A. P.; Leone, S. R.; Yang, P. *J. Am. Chem. Soc.* **2016**, 138, 7236.
- (10) Zhang, D.; Yu, Y.; Bekenstein, Y.; Wong, A. B.; Alivisatos, A. P.; Yang, P. *J. Am. Chem. Soc.* **2016**, 138, 13155.
- (11) Wang, Y.; Bai, L.; Wen, T.; Yang, L.; Gou, H.; Xiao, Y.; Chow, P.; Pravica, M.; Yang, W.; Zhao, Y. *Angew. Chem., Int. Ed.* **2016**, 55, 10350.
- (12) Xiao, G.; Yang, X.; Zhang, X.; Wang, K.; Huang, X.; Ding, Z.; Ma, Y.; Zou, G.; Zou, B. *J. Am. Chem. Soc.* **2015**, 137, 10297.
- (13) Xiao, G.; Wang, K.; Zhu, L.; Tan, X.; Qiao, Y.; Yang, K.; Ma, Y.; Liu, B.; Zheng, W.; Zou, B. *J. Phys. Chem. C* **2015**, 119, 3843.
- (14) Xiao, G.; Zhu, C.; Ma, Y.; Liu, B.; Zou, G.; Zou, B. *Angew. Chem., Int. Ed.* **2014**, 53, 729.
- (15) Jaffe, A.; Lin, Y.; Beavers, C. M.; Voss, J.; Mao, W. L.; Karunadasa, H. I. *ACS Cent. Sci.* **2016**, 2, 201.
- (16) Jaffe, A.; Lin, Y.; Mao, W. L.; Karunadasa, H. I. *J. Am. Chem. Soc.* **2015**, 137, 1673.
- (17) Ou, T.; Yan, J.; Xiao, C.; Shen, W.; Liu, C.; Liu, X.; Han, Y.; Ma, Y.; Gao, C. *Nanoscale* **2016**, 8, 11426.
- (18) Lü, X.; Wang, Y.; Stoumpos, C. C.; Hu, Q.; Guo, X.; Chen, H.; Yang, L.; Smith, J. S.; Yang, W.; Zhao, Y.; Xu, H.; Kanatzidis, M. G.; Jia, Q. *Adv. Mater.* **2016**, 28, 8663.
- (19) Nagaoka, Y.; Hills-Kimball, K.; Tan, R.; Li, R.; Wang, Z.; Chen, O. *Adv. Mater.* **2017**, 29, 1606666.
- (20) Wang, Y.; Lü, X.; Yang, W.; Wen, T.; Yang, L.; Ren, X.; Wang, L.; Lin, Z.; Zhao, Y. *J. Am. Chem. Soc.* **2015**, 137, 11144.
- (21) Wang, L.; Wang, K.; Zou, B. *J. Phys. Chem. Lett.* **2016**, 7, 2556.
- (22) Wang, L.; Wang, K.; Xiao, G.; Zeng, Q.; Zou, B. *J. Phys. Chem. Lett.* **2016**, 7, 5273.
- (23) Li, Q.; Li, S.; Wang, K.; Quan, Z.; Meng, Y.; Zou, B. *J. Phys. Chem. Lett.* **2017**, 8, 500.
- (24) Swainson, I. P.; Tucker, M. G.; Wilson, D. J.; Winkler, B.; Milman, V. *Chem. Mater.* **2007**, 19, 2401.
- (25) Ou, T.; Yan, J.; Xiao, C.; Shen, W.; Liu, C.; Liu, X.; Han, Y.; Ma, Y.; Gao, C. *Nanoscale* **2016**, 8, 11426.
- (26) Liu, G.; Kong, L.; Gong, J.; Yang, W.; Mao, H.; Hu, Q.; Liu, Z.; Schaller, R. D.; Zhang, D.; Xu, T. *Adv. Funct. Mater.* **2017**, 27, 1604208.
- (27) Jiang, S.; Fang, Y.; Li, R.; Xiao, H.; Crowley, J.; Wang, C.; White, T. J.; Goddard, W. A.; Wang, Z.; Baikie, T.; Fang, J. *Angew. Chem., Int. Ed.* **2016**, 55, 6540.
- (28) Szafranski, M.; Katrusiak, A. *J. Phys. Chem. Lett.* **2016**, 7, 3458.
- (29) Mao, H.; Xu, J.-A.; Bell, P. J. *Geophys. Res.* **1986**, 91, 4673.
- (30) Hammersley, A.; Svensson, S.; Hanfland, M.; Fitch, A.; Hausermann, D. *High Pressure Res.* **1996**, 14, 235.
- (31) Clark, S. J.; Segall, M. D.; Pickard, C. J.; Hasnip, P. J.; Probert, M. I.; Refson, K.; Payne, M. C. *Z. Kristallogr. - Cryst. Mater.* **2005**, 220, 567.
- (32) Kresse, G.; Furthmüller, J. *Phys. Rev. B: Condens. Matter Mater. Phys.* **1996**, 54, 11169.
- (33) Zhu, H.; Fu, Y.; Meng, F.; Wu, X.; Gong, Z.; Ding, Q.; Gustafsson, M. V.; Trinh, M. T.; Jin, S.; Zhu, X. Y. *Nat. Mater.* **2015**, 14, 636.
- (34) Wang, T.; Daiber, B.; Frost, J. M.; Mann, S. A.; Garnett, E. C.; Walsh, A.; Ehrler, B. *Energy Environ. Sci.* **2017**, 10, 509.
- (35) Cottingham, P.; Brutchey, R. L. *Chem. Commun.* **2016**, 52, 5246.
- (36) Liu, Q.; Yu, X.; Wang, X.; Deng, Z.; Lv, Y.; Zhu, J.; Zhang, S.; Liu, H.; Yang, W.; Wang, L.; Mao, H.; Shen, G.; Lu, Z.; Ren, Y.; Chen, Z.; Lin, Z.; Zhao, Y.; Jin, C. *J. Am. Chem. Soc.* **2011**, 133, 7892.
- (37) Akira, M.; Kiyotaka, S.; Koichi, S. *Jpn. J. Appl. Phys.* **1993**, 32, 6.
- (38) Yin, W.; Yang, J.; Kang, J.; Yan, Y.; Wei, S. *J. Mater. Chem. A* **2015**, 3, 8926.
- (39) Zhao, X.; Yang, J.; Fu, Y.; Yang, D.; Xu, Q.; Yu, L.; Wei, S.; Zhang, L. *J. Am. Chem. Soc.* **2017**, 139, 2630.
- (40) Wu, B.; Zhou, Y.; Xing, G.; Xu, Q.; Garces, H.; Solanki, A.; Goh, T.; Padture, N.; Sum, T. *Adv. Funct. Mater.* **2017**, 27, 1604818.
- (41) Kong, L. P.; Liu, G.; Gong, J.; Hu, Q. Y.; Schaller, R. D.; Dera, P.; Zhang, D. Z.; Liu, Z. X.; Yang, W. G.; Zhu, K.; Tang, Y. Z.; Wang, C. Y.; Wei, S. H.; Xu, T.; Mao, H. K. *Proc. Natl. Acad. Sci. U. S. A.* **2016**, 113, 8910.